Electronic Supplementary Material (ESI) for Materials Horizons.

— Supplementary Information —

Are Topological Insulators Promising Thermoelectrics?

Michael Y. Toriyama* and G. Jeffrey Snyder*

Materials Science and Engineering, Northwestern University, Evanston, IL 60208, USA.

E-mail: MichaelToriyama2024@u.northwestern.edu; jeff.snyder@northwestern.edu

Computational methods

General details

Density functional theory (DFT) calculations were performed using the Vienna *ab initio* simulation package (VASP).[1–3] The projector-augmented wave (PAW) method[4,5] was used, and the generalized gradient approximation (GGA) following the formalism of Perdew, Burke, and Ernzerhof (PBE)[6] was employed. The energy cutoff was set to 340 eV in all calculations. An on-site Hubbard-U correction[7] was applied following the methodologies of Refs. 8 and 9, where $U = 5$ eV was applied to Cu-d and Ag-d orbitals, and $U = 3$ eV was applied to Au-d orbitals. All structures were relaxed using an automatically-generated k-point mesh with a length factor of 20 Å. The electronic structures were subsequently calculated on the relaxed structures using a Γ-centered mesh, where the equation $N_{\text{kpts}} \approx 8000/N_{\text{atoms}}$ was used to determine the number of k-points sampled in a cell containing N_{atoms} atoms. Spin-orbit coupling (SOC) effects were included in all electronic structure calculations. The SOC strength in DFT calculations was modified using the methodology described in Ref. 10. Fermi surfaces were generated from DFT outputs using the iFermi software.[11]

The M_0 parameter

The M_0 value, as described by Eq. (1) in the main text, was calculated from the electronic structure. The magnitude of M_0 was determined from the energies of the highest occupied and lowest unoccupied states at the Γ-point. Given that all compounds considered in the study are crystal inversion-symmetric, we evaluated the Z_2 invariant from the parity eigenvalues of occupied bands at the time-reversal invariant momenta (TRIM) using the method of Fu and Kane.[12] Since we are considering 3D materials, there are four Z_2 invariants, denoted $(\nu_0;\nu_1\nu_2\nu_3)$. The sign of M_0 is determined from the first Z_2 invariant, ν_0. If $\nu_0 = 0$, then the material is either a normal insulator or a weak TI, the latter of which is analogous to a normal insulator in the presence of disorder. Accordingly, if $\nu_0 = 0$, then we set $M_0 > 0$. If $\nu_0 = 1$ on the other hand, and the wave function symmetries are indeed inverted at the Γ-point, then the compound is a strong TI, and we set $M_0 < 0$. The wave function symmetries to calculate the parity eigenvalues were determined using the irvsp software.[13] The calculated topological characters of compounds considered both in the present study and in the study by Zhang *et al.*[14] are in agreement.

Transport calculations

Detailed transport calculations based on Boltzmann theory were performed using the *Ab initio* Scattering and Transport (AMSET) software.[15] Material parameters required for the DFT transport calculations,

namely the elastic and dielectric tensors, were calculated using the finite difference method and density functional perturbation theory, respectively. The transport properties were obtained by averaging over the three Cartesian directions.

For Bi_2Te_3 and Bi_2Se_3 in particular, we used experimental values for the band gap and lattice thermal conductivity[16] to obtain good agreement with experimentally-measured transport properties. Van der Waals interactions were not included. The calculated properties of Bi_2Te_3 agree well with experimental measurements (Figure S1). The magnitude of the band inversion strength at the Γ-point, $|M_0|$, was evaluated according to the necessary shift in the band gap. For the ZrBeSi-type ABX compounds, we used the band gap calculated using PBE with SOC. The lattice thermal conductivity at 300 K was estimated following the methodology outlined in Refs. 17 and 18. Inputs to the estimation, such as the bulk modulus and mass density, were calculated using DFT. Note that the ABX compounds can host a variety of electronic structures, including insulators with a forbidden band gap and metals/semimetals with no gap.[14] Since we are interested in comparing the thermoelectric properties of insulators (normal and topological), we omit any compounds with zero band gap from our analysis.

Effective masses and weighted mobility

The effective masses and weighted mobility were evaluated from the transport properties calculated using the AMSET software at the band edges (*i.e.*, valence band maximum and conduction band minimum). The Seebeck effective mass m_S^* was evaluated from the Seebeck coefficient S and the carrier concentration n at the band edge in the following way. The reduced Fermi level η was initially determined using the expression

$$S = \frac{k_B}{e}\left(-\eta + \frac{2F_1(\eta)}{F_0(\eta)}\right) \tag{S1}$$

where F_i is the Fermi-Dirac integral

$$F_i(\eta) = \int \frac{\varepsilon^i}{1+\exp(\varepsilon-\eta)} d\varepsilon \tag{S2}$$

We then determine m_S^* using the expression

$$n = 4\pi\left(\frac{2m_S^* k_B T}{h^2}\right)^{3/2} F_{1/2}(\eta) \tag{S3}$$

Note that within a parabolic band assumption, the density of states effective mass m_{DOS}^* is used in Eq. (S3) in place of m_S^* to calculate the carrier concentration. m_{DOS}^* characterizes the number of states available for

charge carriers and is thus a characteristic of the electronic structure of the material. One should interpret the value for m_{S}^{*} calculated in this way as the "effective" number of states involved in transport.[19]

The conductivity effective mass m_{C}^{*} was calculated from σ and the scattering time, similar to the methodology employed in Ref. 20. From the conductivity tensor σ_{ij}, one can evaluate the conductivity mass tensor $m_{\mathrm{C},ij}^{*}$ using the form

$$m_{\mathrm{C},ij}^{*}{}^{-1} = \frac{1}{e^2 \tau n} \sigma_{ij} \tag{S4}$$

where n is the carrier concentration and τ is the scattering time. The key difference between the methodology used in Gibbs *et al.*[20] and the present study lies in the evaluation of τ. As opposed to a constant scattering time $\tau = \tau_0$, an energy-dependent $\tau = \tau(E)$ is computed in this study using the AMSET software. Accordingly, we calculate an *average* scattering time $\langle \tau \rangle$ to evaluate Eq. (S4), using the form[21]

$$\langle \tau \rangle = \frac{\sum_{\mathbf{k}} \tau(E_{\mathbf{k}}) E_{\mathbf{k}} f(E_{\mathbf{k}})}{\sum_{\mathbf{k}} E_{\mathbf{k}} f(E_{\mathbf{k}})} \tag{S5}$$

where a summation over all k-points $\mathbf{k}$ is performed, and $f(E)$ is the Fermi-Dirac distribution. From the tensorial quantity $m_{\mathrm{C},ij}^{*}$, we compute a scalar quantity m_{C}^{*} using a harmonic average:

$$m_{\mathrm{C}}^{*} = 3 \left(\frac{1}{m_{\mathrm{C},x}^{*}} + \frac{1}{m_{\mathrm{C},y}^{*}} + \frac{1}{m_{\mathrm{C},z}^{*}} \right)^{-1} \tag{S6}$$

The weighted mobility μ_w was calculated using the effective masses and average scattering time:

$$\mu_w = \frac{e \langle \tau \rangle}{m_{\mathrm{C}}^{*}} \left(\frac{m_{\mathrm{S}}^{*}}{m_e} \right)^{3/2} \tag{S7}$$

The quality factor B is calculated using μ_w and κ_{L}:

$$B = \left(\frac{k_{\mathrm{B}}}{e} \right)^2 \frac{8\pi e}{3} \left(\frac{2 m_e k_{\mathrm{B}}}{h^2} \right)^{3/2} \frac{\mu_w T^{5/2}}{\kappa_{\mathrm{L}}} \tag{S8}$$

Comparison to experiments for Bi_2Te_3

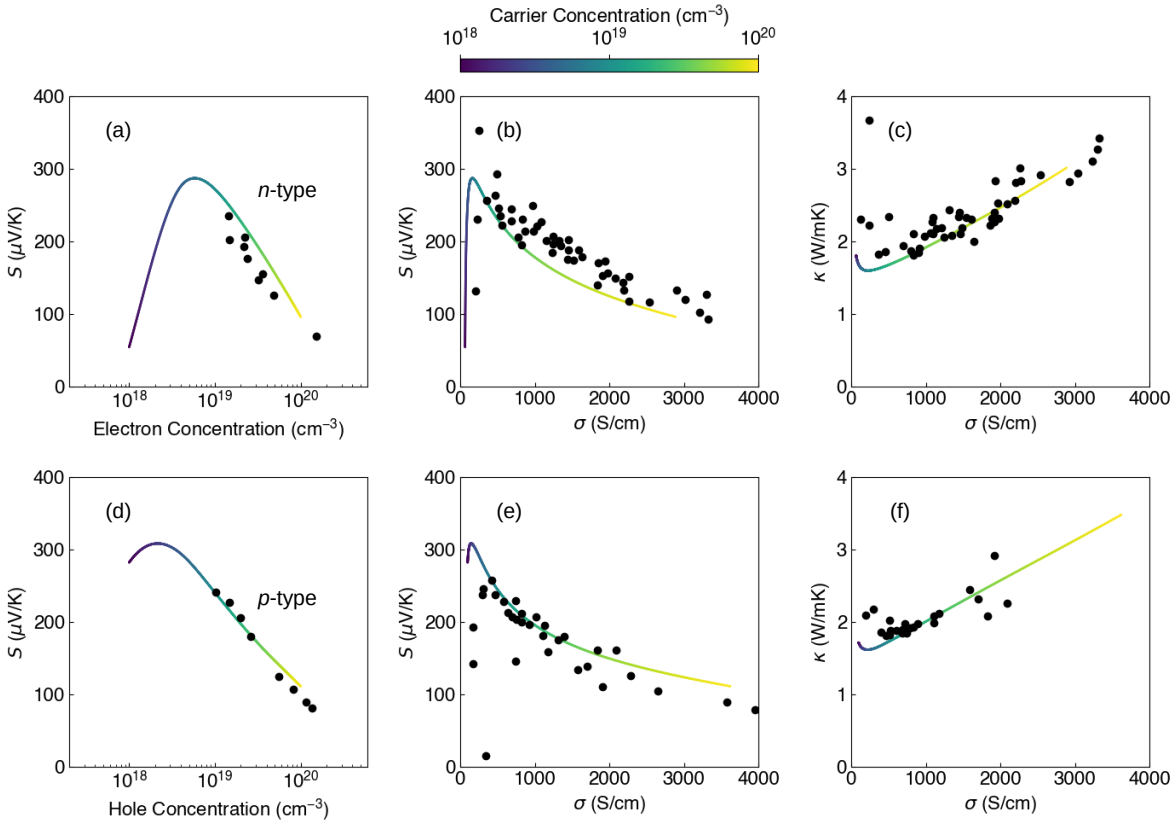

Figure S1: Thermoelectric transport properties of n-type (a-c) and p-type (d-f) Bi_2Te_3, comparing between DFT calculations (solid curves) and experimental measurements (black dots) at 300 K. The experimental values are sourced from Ref. 16 and references therein. We compare the Seebeck coefficient S, electrical conductivity σ, and thermal conductivity κ. The thermal conductivity is the sum of the electronic contribution, calculated using DFT, and the experimental lattice thermal conductivity at 300 K ($\kappa_L = 1.37$ W/mK).[16]

Quality factor B and Fermi surface complexity factor $N_V^* K^*$

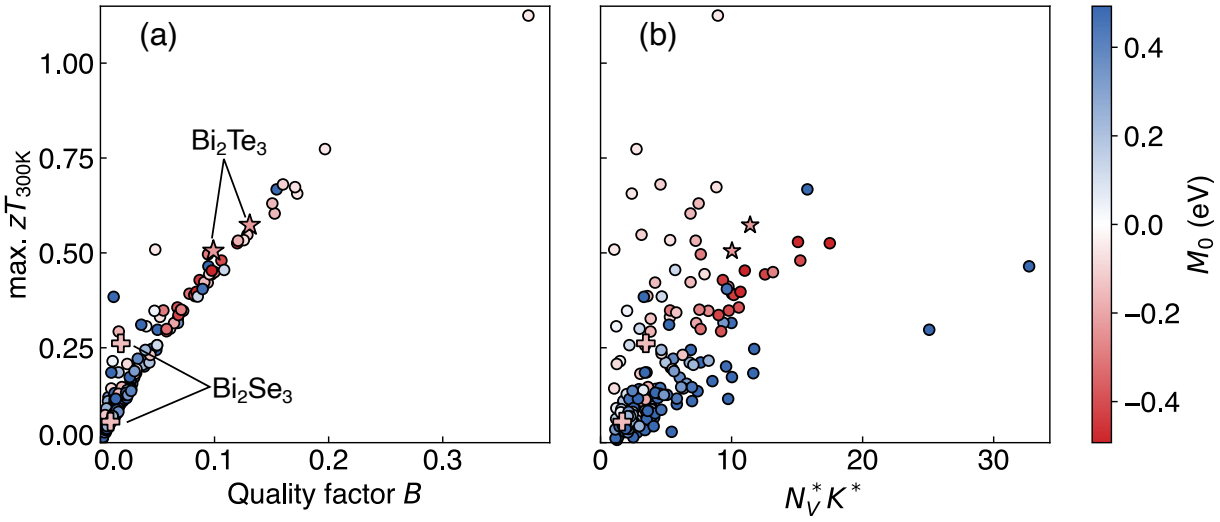

Figure S2: Maximum attainable zT at 300 K, plotted against (a) the quality factor B and (b) the Fermi surface complexity factor $N_V^* K^*$. The color represents M_0, where normal insulators ($M_0 > 0$) are blue and topological insulators ($M_0 < 0$) are red. Bi_2Te_3 and Bi_2Se_3 are denoted by star and plus markers, respectively; the rest are ABX compounds.

Transport model

General Boltzmann transport formalism for isotropic bands

Within the standard Boltzmann transport formalism under the relaxation time approximation,[21–23] the electrical conductivity σ, Seebeck coefficient S, and Lorenz number L for a single isotropic band can be expressed as

$$\begin{aligned}
\sigma &= \int \Sigma(E) \left(-\frac{\partial f}{\partial E}\right) dE \\
S &= \frac{k_\mathrm{B}}{e} \frac{\int \Sigma(E) \left(\frac{E-E_\mathrm{F}}{k_\mathrm{B}T}\right) \left(-\frac{\partial f}{\partial E}\right) dE}{\sigma} \\
L &= \left(\frac{k_\mathrm{B}}{e}\right)^2 \frac{\int \Sigma(E) \left(\frac{E-E_\mathrm{F}}{k_\mathrm{B}T}\right)^2 \left(-\frac{\partial f}{\partial E}\right) dE}{\sigma} - S^2
\end{aligned} \tag{S9}$$

where E_F is the Fermi level and

$$f(E) = \frac{1}{1 + \exp\left(\frac{E-E_\mathrm{F}}{k_\mathrm{B}T}\right)} \tag{S10}$$

is the Fermi-Dirac distribution. The transport function $\Sigma(E)$ of a single band is given as

$$\Sigma(E) = \frac{e^2}{3} v(E)^2 g(E) \tau(E) \tag{S11}$$

which is composed of the carrier velocity $v(E)$, density of states $g(E)$ (DOS), and scattering time $\tau(E)$. The $1/3$ factor manifests from averaging over the three Cartesian directions.

Since topological insulators often possess narrow band gaps, thermoelectric transport can be influenced by bipolar conduction effects from the presence of both majority and minority carriers.[24] We therefore employ a two-band transport model to evaluate the thermoelectric performance, where the transport properties are given as

$$\begin{aligned}
\sigma &= \sigma_e + \sigma_h \\
S &= \frac{S_h \sigma_h - |S_e| \sigma_e}{\sigma} \\
\kappa_e &= L_h \sigma_h T + L_e \sigma_e T + \frac{\sigma_h \sigma_e}{\sigma} \left(S_h + |S_e|\right)^2 T
\end{aligned} \tag{S12}$$

where the subscripts e and h correspond to electrons and holes, respectively. The subscripted transport properties (*e.g.*, σ_e and S_e) are the single-band properties given in Eq. (S9). Note that E_F must be

referenced to the conduction band for electrons and the valence band for holes. More details of the model can be found in Ref. 24.

Warped band transport model

We consider the conduction band within the warped band structure model given in Eq. (3) in the main text, assuming symmetric bands ($C = 0$):

$$E(k) = \sqrt{(M_0 + M_2 k^2)^2 + A^2 k^2} \tag{S13}$$

The transport function $\Sigma(E)$ can be expressed as a sum,

$$\begin{aligned} \Sigma(E) &= \Sigma_O(E) + \Sigma_I(E) \\ &= \frac{e^2}{3} v_O(E)^2 g_O(E) \tau_O(E) + \frac{e^2}{3} v_I(E)^2 g_I(E) \tau_I(E) \end{aligned} \tag{S14}$$

where the subscripts O and I denote the outer and inner Fermi spheres, respectively, for a warped band.

The velocity is defined in terms of the slope of Eq. (S13) with respect to the wave vector

$$\begin{aligned} v &= \frac{1}{\hbar} \frac{dE}{dk} \\ &= \frac{1}{\hbar} \frac{k}{E} \left(2M_0 M_2 + A^2 + 2M_2^2 k^2\right) \end{aligned} \tag{S15}$$

It is useful to express the curvature of the conduction band at $k = k_0$ as a parameter ζ, where

$$\zeta = \frac{2M_0 M_2 + A^2}{|M_0|} \tag{S16}$$

which can be used to re-express the band structure in Eq. (S13) as

$$E(k) = \sqrt{M_0^2 + \zeta |M_0| k^2 + M_2^2 k^4} \tag{S17}$$

and the velocity in Eq. (S15) as

$$v = \frac{1}{\hbar} \frac{k}{E} \left(\zeta |M_0| + 2M_2^2 k^2\right) \tag{S18}$$

As a result, the squared velocity is

$$\begin{aligned} v^2 &= \frac{1}{\hbar^2}\frac{k^2}{E^2}\left((\zeta|M_0|)^2 + 4\zeta|M_0|M_2^2k^2 + 4M_2^4k^4\right) \\ &= \frac{1}{\hbar^2}\frac{k^2}{E^2}\left((\zeta|M_0|)^2 + 4M_2^2\left(E^2 - M_0^2\right)\right) \end{aligned} \tag{S19}$$

From Eq. (S17) we find that

$$k^2 = \frac{-\zeta|M_0| \pm \sqrt{(\zeta|M_0|)^2 + 4M_2^2(E^2 - M_0^2)}}{2M_2^2} \tag{S20}$$

Note that the + and − terms correspond to the outer and inner Fermi spheres, respectively, when the bands are warped ($M_0 < M_{0,c}$). Accordingly, the v^2 terms in Eq. (S14) can be fully expressed in terms of the energy E as

$$\begin{aligned} v_O(E)^2 =& \frac{1}{\hbar^2}\frac{1}{E^2}\left((\zeta|M_0|)^2 + 4M_2^2\left(E^2 - M_0^2\right)\right)\frac{-\zeta|M_0| + \sqrt{(\zeta|M_0|)^2 + 4M_2^2(E^2 - M_0^2)}}{2M_2^2} \\ v_I(E)^2 =& \frac{1}{\hbar^2}\frac{1}{E^2}\left((\zeta|M_0|)^2 + 4M_2^2\left(E^2 - M_0^2\right)\right)\frac{-\zeta|M_0| - \sqrt{(\zeta|M_0|)^2 + 4M_2^2(E^2 - M_0^2)}}{2M_2^2} \end{aligned} \tag{S21}$$

When $E > |M_0|$, the inner Fermi sphere vanishes, which corresponds to $v_I^2 < 0$ and an imaginary v_I.

The DOS for the outer Fermi sphere can be derived from the number of states per volume in 3D

$$n_O = \frac{k_O^3}{3\pi^2} \tag{S22}$$

such that

$$\begin{aligned} g_O(E) &= \frac{dn_O}{dE} \\ &= \frac{k_O^2}{\pi^2}\frac{1}{\hbar v_O} \end{aligned} \tag{S23}$$

where we have invoked $v = \frac{1}{\hbar}\frac{dE}{dk}$. The DOS of the inner Fermi sphere, similarly, is

$$g_I(E) = \frac{k_I^2}{\pi^2}\frac{1}{\hbar v_I} \tag{S24}$$

Note that the total DOS is the sum of contributions from the inner and outer Fermi spheres,

$$g_T(E) = g_O(E) + g_I(E) \tag{S25}$$

The scattering time $\tau(E)$ depends on the dominant mechanism under which charge carriers are scattered. The scattering rate is proportional to the total DOS of the system in many cases, because the phase space into which carriers can scatter scales proportionately with the DOS.[25–27] Accordingly, we model the scattering time for both the inner (τ_I) and outer (τ_O) Fermi spheres as being inversely proportional to the total DOS, *i.e.*

$$\tau_I(E) = \tau_O(E) = \frac{C_{\mathrm{DOS}}}{g_T(E)} \tag{S26}$$

Note that the relationship $\tau(E) \propto g_T(E)^{-1}$ can also be derived assuming scattering by acoustic phonons.[23]

Ultimately, the transport properties within the warped band transport model can be expressed using Eqs. (S9) – (S12), where the warped band transport function in Eq. (S14) takes place of $\Sigma(E)$ in Eq. (S9).

Effective masses from the warped band transport model

The Seebeck effective mass m_{S}^* and conductivity mass m_{C}^* within the warped band transport model are evaluated in a manner similar to the DFT-calculated masses. Namely, m_{S}^* is calculated using Eqs. (S1) – (S3), and m_{C}^* is calculated using Eqs. (S4) – (S6). The only distinction lies in the calculation of the average scattering time $\langle\tau\rangle$. Instead of performing a summation over all $\mathbf{k}$ as in Eq. (S5), an integration is performed:

$$\langle\tau\rangle = \frac{\int \tau(E_{\mathbf{k}}) E_{\mathbf{k}} f(E_{\mathbf{k}}) d\mathbf{k}}{\int E_{\mathbf{k}} f(E_{\mathbf{k}}) d\mathbf{k}} \tag{S27}$$

Multi-valleyed transport model

To model a multi-valleyed electronic structure induced by band inversion, we fit a parabolic band to the band edge of the warped band structure model in Eq. (3) in the main text. We define a parabolic band

$$E = \frac{\hbar^2 k^2}{2m_b^*(\beta)} \tag{S28}$$

where the band effective mass m_b^* is determined from the curvature at the edge of the warped band structure. We use a shorthand notation for the composite variable $\beta \equiv (M_0, A, M_2)$ to indicate which parameters within the multi-valleyed transport model are dependent on features of the warped band structure model.

For N_V parabolic conduction bands (or, equivalently, valence bands), the transport properties arising

from Eq. (S9) follow the forms:

$$\begin{aligned}
\sigma(\eta) &= \frac{8\pi e}{3}\left(\frac{2m_e k_B T}{h^2}\right)^{3/2}\mu_w(\beta)\left(r+\frac{3}{2}\right)F_{r+\frac{1}{2}}(\eta)\\
S(\eta) &= \frac{k_B}{e}\left[-\eta+\frac{r+\frac{5}{2}}{r+\frac{3}{2}}\frac{F_{r+\frac{3}{2}}(\eta)}{F_{r+\frac{1}{2}}(\eta)}\right]\\
L(\eta) &= \left(\frac{k_B}{e}\right)^2\left[\frac{r+\frac{7}{2}}{r+\frac{3}{2}}\frac{F_{r+\frac{5}{2}}(\eta)}{F_{r+\frac{1}{2}}(\eta)}-\left(\frac{r+\frac{5}{2}}{r+\frac{3}{2}}\frac{F_{r+\frac{3}{2}}(\eta)}{F_{r+\frac{1}{2}}(\eta)}\right)^2\right]
\end{aligned} \tag{S29}$$

where μ_w is the weighted mobility given as

$$\begin{aligned}
\mu_w(\beta) &= \mu_0(\beta)\left(\frac{m^*_{\mathrm{DOS}}(\beta)}{m_e}\right)^{3/2}\\
&= \frac{e\tau_0(\beta)}{m^*_b(\beta)}N_V\left(\frac{m^*_b(\beta)}{m_e}\right)^{3/2}
\end{aligned} \tag{S30}$$

The scattering time prefactor, $\tau_0(\beta)$, in Eq. (S30) arises from the assumption that the scattering time $\tau(E)$ in Eq. (S11) follows a power-law form

$$\tau = \tau_0\left(\frac{E}{k_B T}\right)^r \tag{S31}$$

In order to have the results for the multi-valleyed transport model be comparable to those of the warped band transport model, we determine the form of τ_0 such that Eq. (S31) matches the form of Eq. (S26) when $r = -1/2$. The scattering parameter r is chosen according to the assumed scattering mechanism, where $r = -1/2$ represents scattering that is proportional to the phase space (*i.e.* $1/\tau \sim g_T(E)$).[27] Accordingly, we determine from Eqs. (S26) and (S31) that

$$\begin{aligned}
\tau_0(\beta) &= \frac{C_{\mathrm{DOS}}}{g_T(E)}\left(\frac{E}{k_B T}\right)^{1/2}\\
&= C_{\mathrm{DOS}}\frac{\pi^2\hbar^3}{\sqrt{2}N_V(\beta)\left(m^*_b(\beta)\right)^{3/2}}\frac{1}{(k_B T)^{1/2}}
\end{aligned} \tag{S32}$$

where C_{DOS} is the same as in Eq. (S26). The weighted mobility in Eq. (S30) can then be re-expressed as

$$\mu_w(\beta) = C_{\mathrm{DOS}}\frac{e\pi^2\hbar^3}{m_e^{3/2}(2k_B T)^{1/2}}\frac{1}{m^*_b(\beta)} \tag{S33}$$

The assumed scattering mechanism implies that μ_w is agnostic of the specific number of carrier pockets N_V that emerge from band inversion-induced warping. Accordingly, at a constant Fermi level and temperature (*i.e.* constant η), the thermoelectric transport properties do not change with N_V. Note that the same

conclusion may not hold when a different scattering mechanism dominates thermoelectric transport.

The carrier concentration, however, depends on N_V in general. In this study, we consider materials where warping leads to a valley degeneracy of 6, such as Bi_2Te_3. Accordingly, we define

$$N_V(\beta) = \begin{cases} 6 & \text{if } M_0 < M_{0,c} \\ 1 & \text{otherwise} \end{cases} \tag{S34}$$

It is convenient to express the band gap, $E_g(\beta)$, in terms of the band edge position. The band edge relative to mid-gap, $E_b(\beta)$, depends on whether the bands are warped or not. If the bands are not warped ($M_0 \geq M_{0,c}$) and are therefore single-valleyed, then E_b is determined at the k-point where band inversion occurs (k_0). Otherwise, E_b is determined at a k-point away from k_0, say $k_{\mathrm{B}}(\beta)$, which can be expressed as

$$k_{\mathrm{B}}(\beta)^2 = \frac{-2M_0M_2 - A^2}{2M_2^2} \tag{S35}$$

Correspondingly, we can express $E_b(\beta)$ as

$$E_b(\beta) = \begin{cases} A\sqrt{-\frac{M_0}{M_2} - \left(\frac{A}{2M_2}\right)^2} & \text{if } M_0 < M_{0,c} \\ |M_0| & \text{otherwise} \end{cases} \tag{S36}$$

and the band gap

$$E_g(\beta) = 2E_b(\beta) \tag{S37}$$

for both cases. The effective mass $m_b^*(\beta) = \hbar^2 / \left(\frac{\partial^2 E}{\partial k^2}\right)$ can be expressed in terms of $E_b(\beta)$:

$$m_b^*(\beta) = \begin{cases} \frac{\hbar^2 E_b(\beta)}{-4M_0M_2 - 2A^2} & \text{if } M_0 < M_{0,c} \\ \frac{\hbar^2 E_b(\beta)}{2M_0M_2 + A^2} & \text{otherwise} \end{cases} \tag{S38}$$

Model parameters

For the results of the model in Figures 5 and 6 in the main text, the lattice thermal conductivity was set to $\kappa_{\mathrm{L}} = 1$ W/mK. We set the band structure parameters to $C = 0$ eV Å^2, $A = 1.5$ eV Å , and $M_2 = 20$ eV Å^2. We set the coefficient for the scattering time $C_{\mathrm{DOS}} = 1 \times 10^{32}$ J^{-1}m^{-3}s.

zT within the parameter space of the band structure model

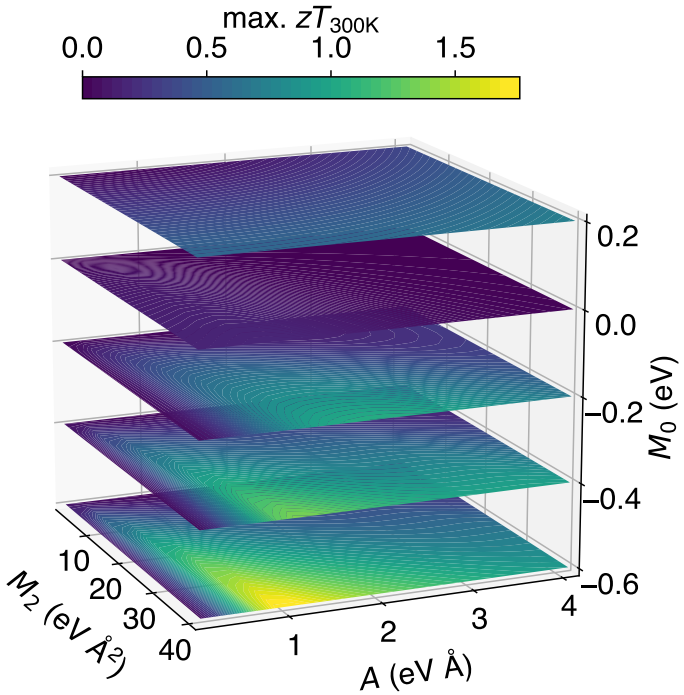

Figure S3: Maximum attainable zT at 300 K (denoted "max. zT_{300K}") calculated using the warped band transport model. The parameter space of the band structure model in Eq. (S13) is explored. In general, regardless of the first- and second-order corrections to the band structure (A and M_2, respectively), the maximum zT is higher when the bands are more inverted (*i.e.*, more negative M_0).

Transport properties from the warped band transport model

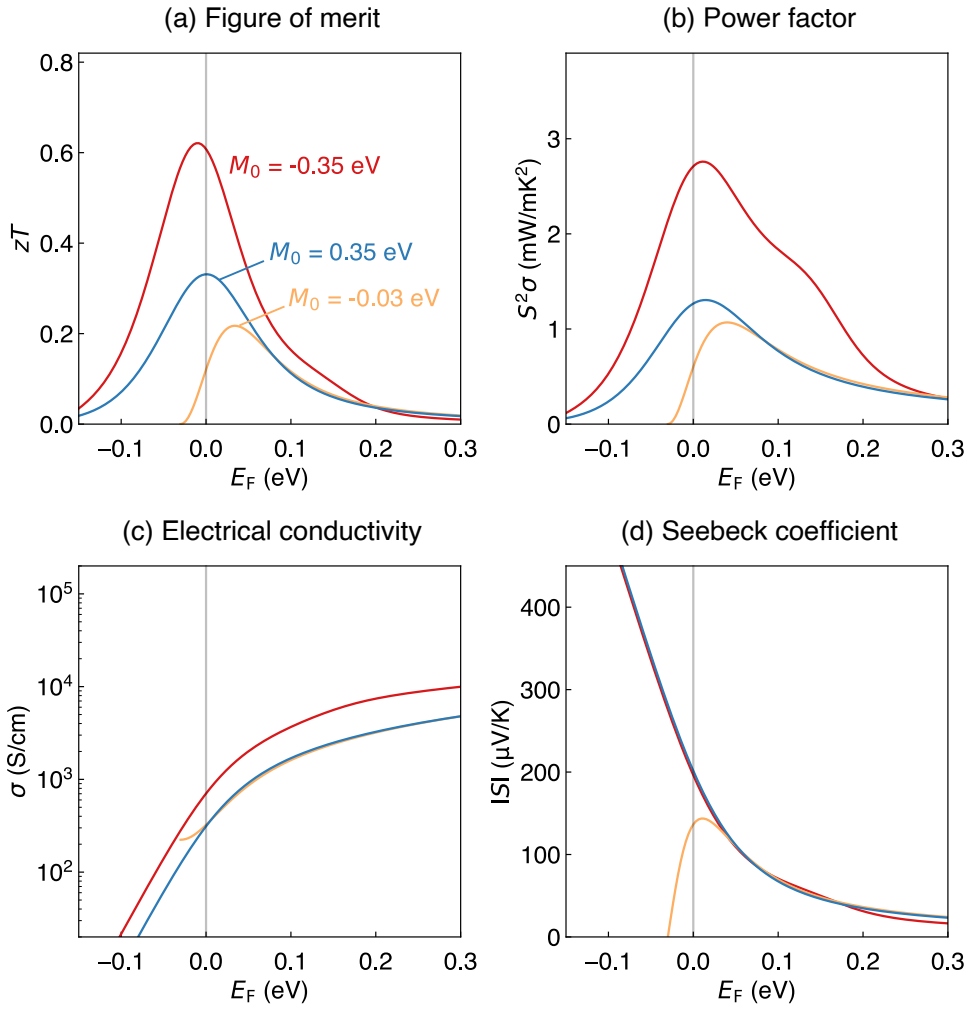

Figure S4: Properties from the warped band transport model, namely (a) zT, (b) power factor, (c) electrical conductivity, and (d) Seebeck coefficient, plotted as a function of Fermi level referenced to the band edge. Three representative band structures are considered: non-inverted ($M_0 = 0.35$ eV, blue), inverted and single-valleyed (M_0 = -0.03 eV, yellow), and inverted but warped (M_0 = -0.35 eV, red).

Transport properties from the multi-valleyed transport model

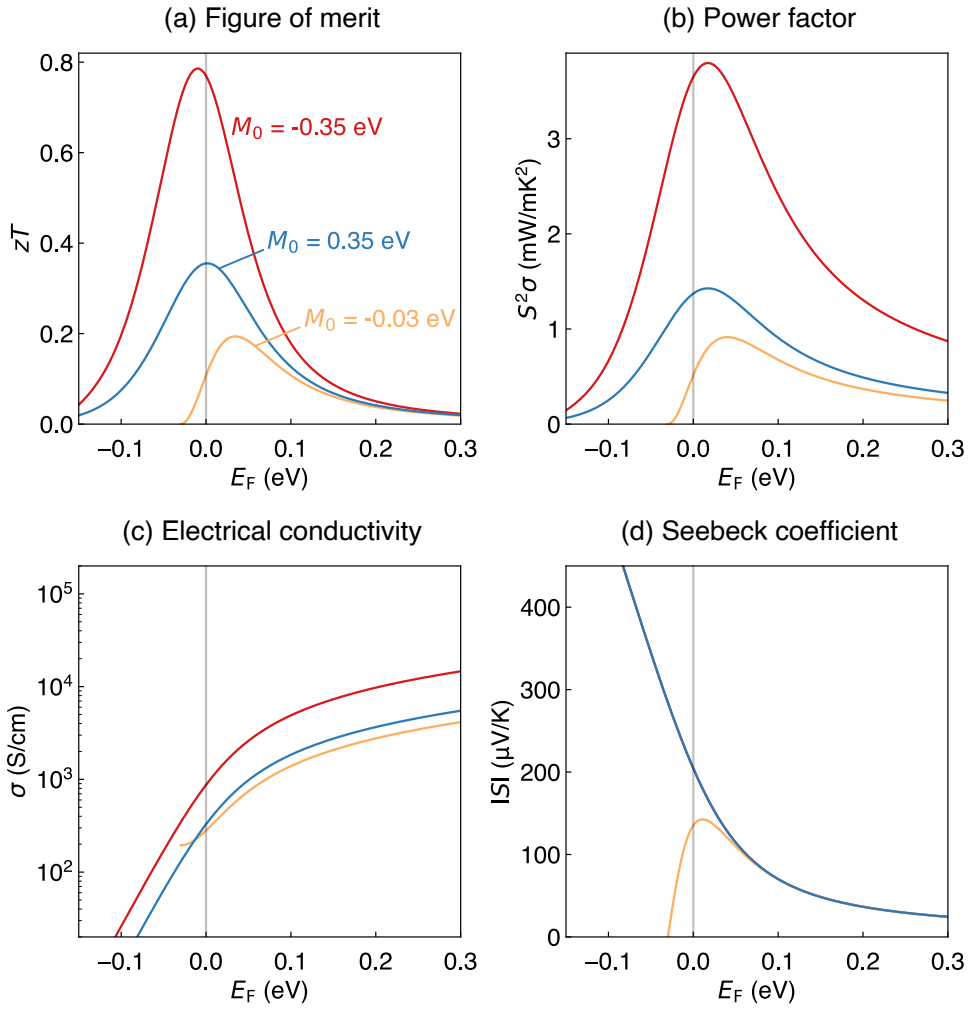

Figure S5: Properties from the multi-valleyed transport model, namely (a) zT, (b) power factor, (c) electrical conductivity, and (d) Seebeck coefficient, plotted as a function of Fermi level referenced to the band edge. Three representative band structures are considered: non-inverted ($M_0 = 0.35$ eV, blue), inverted and single-valleyed (M_0 = -0.03 eV, yellow), and inverted but warped (M_0 = -0.35 eV, red).

Effects of spin-orbit coupling on the band structure of Bi_2Se_3

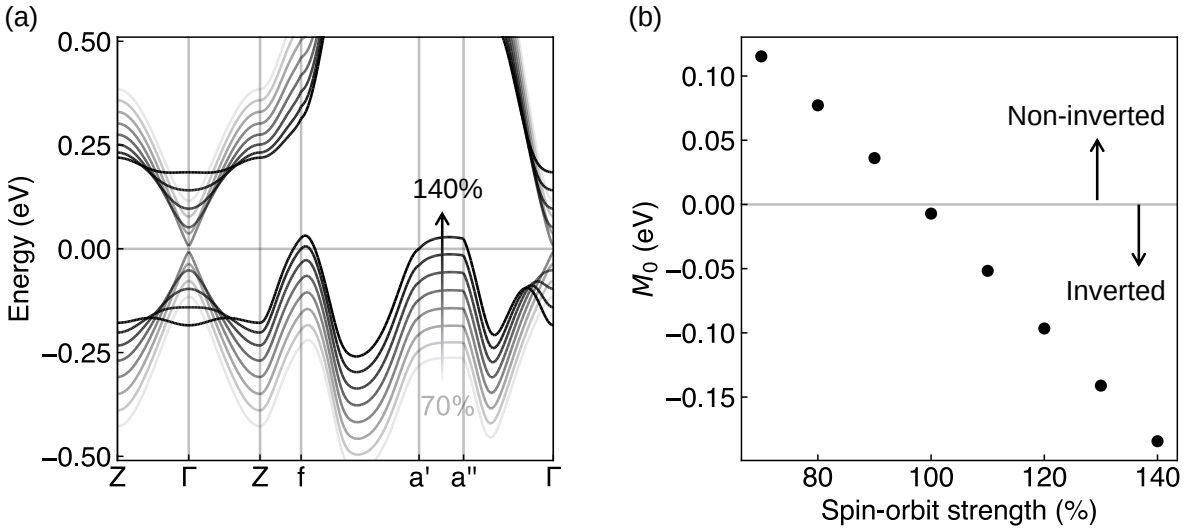

Figure S6: Calculated (a) band structure and (b) M_0 by varying the spin-orbit coupling strength in Bi_2Se_3. The spin-orbit strength is listed relative to the normal amount at 100%, varied from 70% (lightest shade) to 140% (darkest shade). The corresponding M_0 is calculated at the Γ-point.

Effects of strain on the band structure of Bi_2Te_3

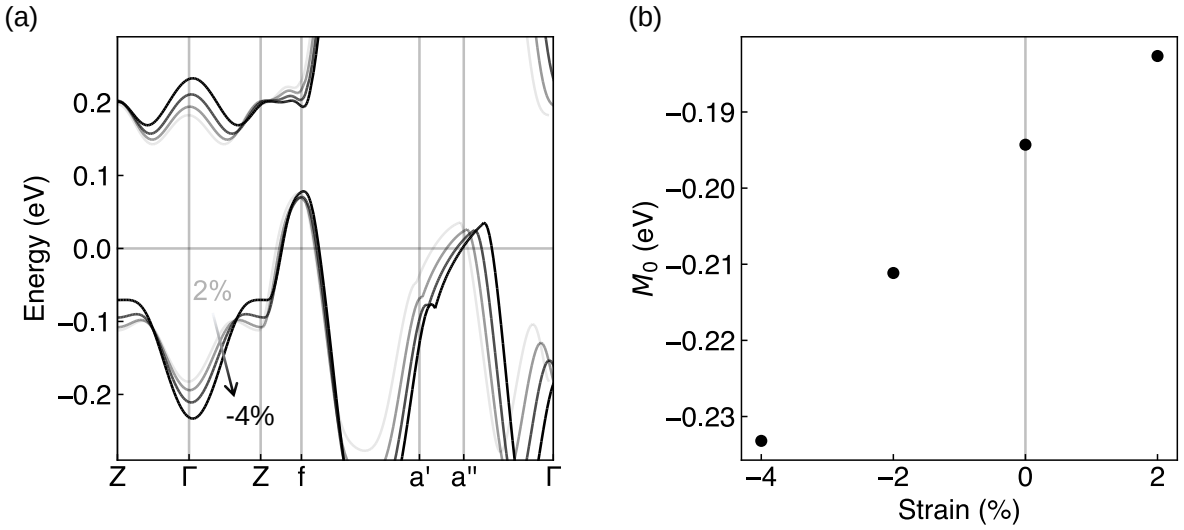

Figure S7: Calculated (a) band structure and (b) M_0 by hydrostatically straining Bi_2Te_3. The strain is listed relative to the DFT-relaxed lattice parameters, varied from 2% (tensile strain, lightest shade) to -4% (compressive strain, darkest shade). The corresponding M_0 is calculated at the Γ-point.

References

(1) Kresse, G. Ab initio molecular dynamics for liquid metals. *J. Non-Cryst. Solids* **1995**, *192*, 222.

(2) Kresse, G.; Furthmüller, J. Efficiency of ab-initio total energy calculations for metals and semiconductors using a plane-wave basis set. *Comp. Mater. Sci.* **1996**, *6*, 15.

(3) Kresse, G.; Furthmüller, J. Efficient iterative schemes for ab initio total-energy calculations using a plane-wave basis set. *Phys. Rev. B* **1996**, *54*, 11169.

(4) Blöchl, P. E. Projector augmented-wave method. *Phys. Rev. B* **1994**, *50*, 17953.

(5) Kresse, G.; Joubert, D. From ultrasoft pseudopotentials to the projector augmented-wave method. *Phys. Rev. B* **1999**, *59*, 1758.

(6) Perdew, J. P.; Burke, K.; Ernzerhof, M. Generalized gradient approximation made simple. *Phys. Rev. Lett.* **1996**, *77*, 3865.

(7) Dudarev, S.; Botton, G.; Savrasov, S.; Humphreys, C.; Sutton, A. Electron-energy-loss spectra and the structural stability of nickel oxide: An LSDA+ U study. *Phys. Rev. B* **1998**, *57*, 1505.

(8) Stevanović, V.; Lany, S.; Zhang, X.; Zunger, A. Correcting density functional theory for accurate predictions of compound enthalpies of formation: Fitted elemental-phase reference energies. *Phys. Rev. B* **2012**, *85*, 115104.

(9) Gorai, P.; Toberer, E. S.; Stevanović, V. Thermoelectricity in transition metal compounds: the role of spin disorder. *Phys. Chem. Chem. Phys.* **2016**, *18*, 31777.

(10) Toriyama, M. Y.; Snyder, G. J. Band inversion-driven warping and high valley degeneracy. *Cell Rep. Phys. Sci.* **2023**, *4*, 101392.

(11) Ganose, A. M.; Searle, A.; Jain, A.; Griffin, S. M. IFermi: A python library for Fermi surface generation and analysis. *J. Open Source Softw.* **2021**, *6*, 3089.

(12) Fu, L.; Kane, C. L. Topological insulators with inversion symmetry. *Phys. Rev. B* **2007**, *76*, 045302.

(13) Gao, J.; Wu, Q.; Persson, C.; Wang, Z. Irvsp: to obtain irreducible representations of electronic states in the VASP. *Comput. Phys. Commun.* **2021**, *261*, 107760.

(14) Zhang, X.; Liu, Q.; Xu, Q.; Dai, X.; Zunger, A. Topological insulators versus topological Dirac semimetals in honeycomb compounds. *J. Am. Chem. Soc.* **2018**, *140*, 13687.

(15) Ganose, A. M.; Park, J.; Faghaninia, A.; Woods-Robinson, R.; Persson, K. A.; Jain, A. Efficient calculation of carrier scattering rates from first principles. *Nat. Commun.* **2021**, *12*, 1.

(16) Witting, I. T.; Chasapis, T. C.; Ricci, F.; Peters, M.; Heinz, N. A.; Hautier, G.; Snyder, G. J. The thermoelectric properties of bismuth telluride. *Adv. Electron. Mater.* **2019**, *5*, 1800904.

(17) Yan, J.; Gorai, P.; Ortiz, B.; Miller, S.; Barnett, S. A.; Mason, T.; Stevanović, V.; Toberer, E. S. Material descriptors for predicting thermoelectric performance. *Energ. Environ. Sci.* **2015**, *8*, 983.

(18) Miller, S. A.; Gorai, P.; Ortiz, B. R.; Goyal, A.; Gao, D.; Barnett, S. A.; Mason, T. O.; Snyder, G. J.; Lv, Q.; Stevanović, V.; Toberer, E. S. Capturing anharmonicity in a lattice thermal conductivity model for high-throughput predictions. *Chem. Mater.* **2017**, *29*, 2494.

(19) Snyder, G. J.; Pereyra, A.; Gurunathan, R. Effective mass from seebeck coefficient. *Adv. Funct. Mater.* **2022**, *32*, 2112772.

(20) Gibbs, Z. M.; Ricci, F.; Li, G.; Zhu, H.; Persson, K.; Ceder, G.; Hautier, G.; Jain, A.; Snyder, G. J. Effective mass and Fermi surface complexity factor from ab initio band structure calculations. *npj Comput. Mater.* **2017**, *3*, 8.

(21) Lundstrom, M. Fundamentals of carrier transport. 2002.

(22) Ashcroft, N. W.; Mermin, N. D. *Solid State Physics*; Cengage Learning, 1976; Vol. 3.

(23) Askerov, B. M. *Electron transport phenomena in semiconductors*; World scientific, 1994.

(24) Toriyama, M. Y.; Carranco, A. N.; Snyder, G. J.; Gorai, P. Material descriptors for thermoelectric performance of narrow-gap semiconductors and semimetals. *Mater. Horiz.* **2023**, *10*, 4256.

(25) Witkoske, E.; Wang, X.; Lundstrom, M.; Askarpour, V.; Maassen, J. Thermoelectric band engineering: The role of carrier scattering. *J. Appl. Phys.* **2017**, *122*, 175102.

(26) Rudderham, C.; Maassen, J. Analysis of simple scattering models on the thermoelectric performance of analytical electron dispersions. *J. Appl. Phys.* **2020**, *127*, 065105.

(27) Askarpour, V.; Maassen, J. First-principles analysis of intravalley and intervalley electron-phonon scattering in thermoelectric materials. *Phys. Rev. B* **2023**, *107*, 045203.